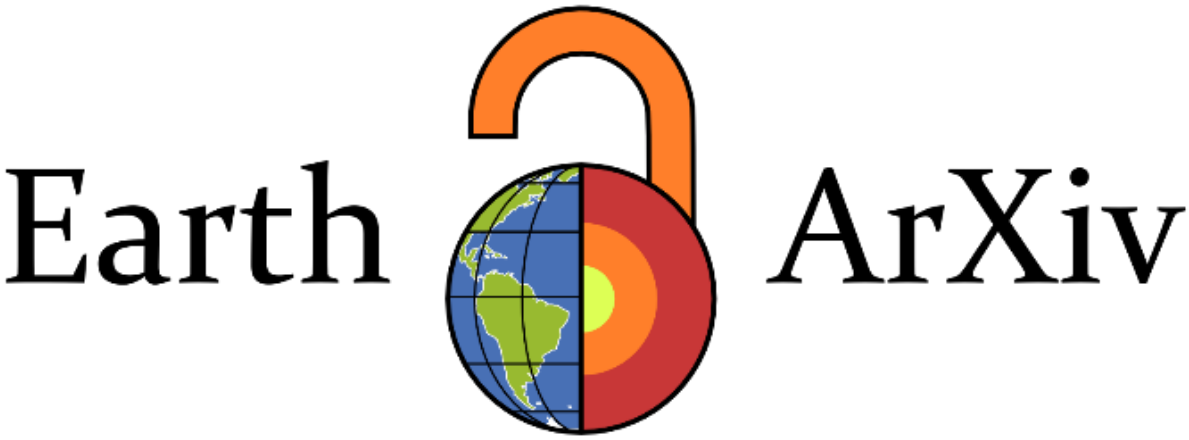

Long-term magma recharge episodes recorded in plagioclase zoning in the Okama pyroclastics at Zao Volcano, northeastern Japan

Motohiro Sato*[1,2], Masao Ban[3], Ryuichi Shinjo[4], Ke-Han Song[4], Takashi Yuguchi[5], Tatsuya Adachi[2], and Takumi Imura[3]

[1] Sabo & Landslide Technical Center, SABO-Kaikan 5F, 2-7-5, Hirakawa-cho, Chiyoda-ku, Tokyo 102-0093, Japan

[2] Graduate School of Science and Engineering, Yamagata University, 1-4-12, Kojirakawa-machi, Yamagata 990-8560, Japan

[3] Faculty of Science, Yamagata University, 1-4-12, Kojirakawa-machi, Yamagata 990-8560, Japan

[4] Graduate School of Engineering and Science, University of the Ryukyus, 1-Senbaru, Nakagami District, Nishihara, Okinawa 903-0213, Japan

[5] Faculty of Science, Kumamoto University, 2-39-1, Kurokami, Chuo-ku, Kumamoto-shi, Kumamoto 860-8555, Japan

* msatores@gmail.com [corresponding author]

ORCiD (1st author): 0000-0002-3057-8570

ORCiD (2nd author): 0000-0002-8872-3339

ORCiD (3rd author): 0000-0001-7087-8773

ORCiD (5th author): 0000-0002-6541-1615

ORCiD (7th author): 0000-0001-6082-6865

Keywords: Mafic magma recharge; Crystal mush; Diffusion chronometry; CaAl–NaSi interdiffusion; Magma batch; Plagioclase

Abstract

Mafic magma recharge into shallow plumbing systems is one of the most important processes for remobilizing crystal mush-dominated magma reservoirs, eventually triggering eruptions. Previous studies have mainly focused on pre-eruptive recharge episodes, revealing short mixing-to-eruption timescales through diffusion chronometry applied to fast-diffusing elements. However, the existence of complexly zoned crystals, commonly observed in arc intermediate magmas, implies multiple recharge episodes. Long-term variations in the rate of mafic magma supply remain unclear, hindering the interpretation of geophysical monitoring data during unrest. Here, we present plagioclase residence timescales from pyroclastic deposits associated with the historical activity at Zao Volcano, northeastern Japan. Compositional zoning patterns of anorthite content within plagioclase crystals record the long-term evolution of magmatic processes due to the slow diffusivity of CaAl–NaSi interdiffusion. The wide diversity of zoning complexities observed at the thin-section scale indicates the remobilization of mushy reservoirs within spatially restricted regions. The distribution of diffusion timescales derived from CaAl–NaSi and Sr in plagioclase reveals that mafic magmas continuously recharged the shallow reservoirs from approximately 100 years before eruption until shortly before the onset. These long-term mixing episodes highlight the importance of continuous monitoring in active arc volcanoes.

1. Introduction

In an intermediate magmatic system beneath arc volcanoes, magmas formed in the lower crust ascend buoyantly and are stored in an upper crustal magma reservoir (e.g. Annen et al., 2006). Cooling magma stored in the upper crustal levels is thermally buffered by latent heat release and spends most of its lifetime at temperatures above a critical crystallinity (40–50 vol%) at which magma is uneasily mobilized (Marsh, 1996; Bachmann and Bergantz, 2006; Cashman et al., 2017; Rubin et al., 2017). Such highly-crystallized magma reservoir, crystal mush, can be ephemerally rejuvenated by arrival of hot, volatile-rich magma recharge, which remobilize the stagnant mushy reservoir, consequently triggering volcanic eruptions (e.g. Sparks et al., 1977; Kent et al., 2010).

Zao Volcano is located in the central part of the volcanic front of northeastern Japan arc (Figure 1). Its activity is subdivided into six stages (Stages I–VI) (Ban et al., 2015). Tephrochronological study revealed that activity of the latest stage (Stage VI) commenced at 35 ka. The activity from the latest crater lake, Okama, started at approximately 1200 CE. The eruption products are small-scale (VEI 1–2) phreatic and phreatomagmatic pyroclastic deposits. Although the eruption products during the activity of Okama crater, hereinafter referred to as Okama pyroclastics (Okp), are remarkably restricted in the whole-rock composition (~57 wt% SiO_2) during the six subunits (Okp-1 to 6), disequilibrium mineral textures and assemblages are observed (Ban et al., 2016; Sato et al., 2022, 2025). This monotonous petrological feature is commonly observed in eruption products erupted from other northeastern Japan arc volcanoes (e.g. Azumayama volacno: Ban et al., 2026), suggesting that magma mixing plays an important role in petrogenesis of andesitic systems at subduction zone volcanoes.

A key unknown is frequency and duration of magma intrusions that lead magma stored in the shallow reservoirs to eruptions. Magma recharge episodes are recorded by crystals as textural and compositional zoning, and the elapsed time from growth of zoning at modified magmatic conditions to quenches by eruptions can be constrained by diffusion chronometry applied to these compositional zoning. Previous studies have constrained mixng-to-eruption timescales using Fe–Mg in pyroxene (Sato et al., 2022) and Mg in plagioclase (Sato et al., 2025). Existence of complexly zoned crystals suggests multiple recharge episodes as well as pre-eruptive recharge. Hitherto, diffusion chronometry studies employing fast diffusive components, have focused on magma recharge episodes immediately prior to eruption; however, longer-term intrusion frequency and duration have been poorly constrained.

Here, we use diffusion chronometry of CaAl–NaSi and Sr in plagioclase derived from the Okp eruption products, to show that eruptions are closely linked with long-term multiple recharge episodes into a shallow magma reservoir. Anorthite [An = 100 × Ca/(Ca + Na + K)] content in plagioclase are good archives of the long-term magmatic processes, owing to the slow diffusivity (Grove et al., 1984; Liu and Yund, 1992) compared with other components including Ti in Fe-Ti oxide minerals (Van Orman and Crispin, 2010), Mg in plagioclase (Costa et al., 2003; Faak et al., 2013; Van Orman et al., 2014), Fe–Mg in pyroxene (Ganguly and Tazzoli, 1994; Müller et al., 2013; Dohmen et al., 2016), and Fe–Mg in olivine (Dohmen and Chakraborty, 2007). Although CaAl–NaSi interdiffusion has been only applied to mid-ocean ridge basalts (Zhang et al., 2015), its application to subduction zone andesites remains unexplored. Mixing-to-eruption timescales constrained by diffusion modelling of CaAl–NaSi in plagioclase crystals can reconstruct the decadal- to century-scale duration and frequency of recharge episodes.

2. Methods and materials

Samples were collected from juvenile scoriae that erupted from 1200 CE to 1897 CE on the latest crater lake of Zao Volcano (Sato et al., 2022) (Supplementary Material). The mineral assemblage consists of plagioclase + orthopyroxene + clinopyroxene + Fe-Ti oxides ± olivine, with phenocryst sizes ranging from mesocryst to macrocryst (Zellmer, 2021). The whole-rock compositions were plotted into medium-K, calc-alkaline basaltic andesite to andesite (~57 mass% SiO_2), whereas the matrix compositions were andesite to dacite (~63 mass% SiO_2). The detailed petrological observation results are reported in Sato et al. (2022).

Back-scattered electron (BSE) images were obtained using a JEOL IT-100 scanning electron microscope (SEM) at Yamagata University. Imaging conditions were an accelerating voltage of 15 kV, working distance of 10 mm, and a beam current of 1.0 nA. Magnification was set to 300x–500x (0.08–0.05 μm/pixel as image resolution). Greyscale intensity of BSE images was quantified using an open-source software, ImageJ (https://imagej.net/ij/). The major and minor elements in plagioclase were analysed using a JEOL JXA-8900R wavelength-dispersive electron probe microanalyser (EPMA) at Yamagata University. Analytical conditions were an accelerating voltage of 15 kV, a beam current of 10 nA, and a defocused beam (~10 μm diameter). Peak counting times for major (Si, Al, Ca, Na, and K) and minor (Mg and Fe) were 10 s and 60 s, respectively. Na and K were first analysed to reduce alkaline migration during irradiation.

The Sr in plagioclase was analysed using a laser ablation inductively coupled plasma mass spectrometry (LA-ICP-MS) at the University of the Ryukyus. The analytical methods followed Deevsalar et al. (2023). The USGS glass sample (BHVO-2G) was used as a standard material. The analytical uncertainty was validated using the USGS glass samples (BCR-2G and BIR-1G). Anorthite crystal from Miyake-jima volcano (MKPL) (Kimura and Chang, 2012) was used as a secondary standard material.

3. Results

3.1. Plagioclase characteristics and origins

Complex texturally and compositionally zoned plagioclase crystals are ubiquitous in the Okp eruption products (Figure 2). In our previous study (Sato et al., 2025), the Okp plagioclase was subdivided into four types based on their core textures, oscillatory-zoned (Type A), patchy (Type B), coarsely sieved (Type C), and honeycomb (Type D). Among the subunits of Okp-1 to Okp-6, the proportions of types A, B, C, and D plagioclase crystals range from 4%–10% (mean 7%), 50%–78% (mean 64%), 8%–37% (mean 24%), and 0%–8% (mean 6%), respectively (Sato et al., 2025). The oscillatory-zoned core originates from the cyclic changes of magmatic conditions, indicating repeated recharge of mafic magmas. The patchy core generally showed the remnant of oscillatory-zoned core, indicating the resorption of pre-existing crystals. Coarsely sieved core indicates the crystal resorption (Viccaro et al., 2010). Its high-An content ($An_{>75}$) implies that the resorption occurred by decompression melting rather than magma mixing. The honeycomb cores were formed by rapid growth (Kawamoto, 1992).

Even within the same phenocryst type, the Okp plagioclase showed diverse zoning patterns. Type A plagioclase phenocrysts showed mantle-less and dusty-zoned mantle, whose texture was formed by interaction with Ca-rich melt (Tsuchiyama, 1985). Type B plagioclase phenocrysts showed mantle-less, and oscillatory-zoned, and dusty-zoned mantles. Type C plagioclase phenocrysts showed mantle-less. Type D plagioclase phenocrysts showed mantle-less and homogeneous mantle. Regardless of these core types, plagioclase phenocrysts were predominantly

overgrown by homogeneous rims. The unimodal compositional distribution of crystal rims indicates that the magmas were assembled from various regions and finally mixed.

The Sr and Mg contents in plagioclase were 400–600 μg/g and 0.05–0.15 mass%, showing positive and negative correlation with An content. In the dusty-zoned mantles, both Mg and An contents were exceptionally enriched. The moderate An contents of type A, B, and C plagioclase cores imply they derived from an intermediate magma. The An contents in these cores overlap with those in homogeneous rims that are assumed to be in equilibrium with the eruptive melt. The prevalence of absorbed and dissociated textures indicates the resorption by the injection of hotter or Ca-rich melt. Type D plagioclase only shows normal zoning, thereby derived from the mafic source. The Types A, B, and C phenocrysts were likely derived from the shallow reservoir, whereas the Type D phenocrysts were derived from the recharged magma.

3.2. Timescale modelling

3.2.1. CaAl–NaSi interdiffusion

CaAl–NaSi interdiffusion in plagioclase was modelled for 228 zoning boundaries in 51 plagioclase crystals (Table 1; Supplementary Material). To obtain plagioclase crystals for diffusion modelling systematically, we sampled crystals intersecting an equally spaced grid overlaid on the thin sections. A strong positive linear relationship between BSE greyscale intensity and An content has been reported (Cashman and Blundy, 2013), and therefore the zoning observed in BSE images was inferred to reflect the An content accurately. This relationship allows compositional profiles in An content to be examined at a high spatial resolution compared with EPMA spot analysis (10 μm in diameter). In addition, BSE imaging enables the rapid acquisition of a large number of profiles. Greyscale intensity profiles were analysed perpendicular to the zoning boundaries. A sectioning effects can anomalously stretch profiles, resulting in the overestimation of diffusion time. Where possible, we took more than one profile per zoning boundary and used the sharpest and most symmetrical profile for modelling.

The initial profiles were assumed to be stepwise functions, and the values were estimated from the compositional plateau of An content (e.g. Figure 4). Diffusion coefficients were taken from the experimental results on bytownite ($An_{70–90}$) under hydrous conditions at 900–1050 °C (Liu and Yund, 1992):

$$D_{\mathrm{CaAl-NaSi}} = 4 \times 10^{-16} exp\left(\frac{-103000}{RT}\right)$$

where R is the gas constant (8.314 J $mol^{-1}K^{-1}$), and T is temperature (in Kelvin). Modelling was performed via the analytical solution of Fick's second law (Crank, 1976; Costa and Morgan, 2010):

$$C_{(x,t)} = C_0 + \frac{(C_1 - C_0)}{2} \mathrm{erfc}\left(\frac{x}{2\sqrt{Dt}}\right)$$

where $C_{(x,t)}$ is the An content at the distance from the boundary x at time t, C_0 and C_1 are the initial compositions on each side of the boundary, and D is the diffusion coefficient in m^2s^{-1}. The modelled profiles were fitted using a liner least-squares method. The input magmatic temperature was ~1025 °C, estimated by the orthopyroxene–liquid thermometer (Putirka, 2008) applied to the pairs of orthopyroxene rim and matrix composition (Sato et al., 2022). Given uncertainties of ±30 °C in temperature estimates, the calculated timescales yield shorter and longer uncertainties of −50% and +100% as relative values, respectively. The constraining limitation of timescales is less

than 25 days based on the calculated diffusion coefficients and spatial resolution of BSE images. The CaAl–NaSi interdiffusion modelling result spans from a few years to 100 years (Table 1; Figure 3; Figure 4).

3.2.2. Sr diffusion

We validated the CaAl–NaSi interdiffusion timescales using a comparison with the Sr diffusion timescales. The application of Sr diffusion modelling to finely and complexly zoned plagioclase crystals is limited by the coarse spatial resolution of LA-ICP-MS analysis. We therefore estimated entire diffusion timescales within crystals rather than individual zoning boundaries (Figure 6; Figure 7).

We used the Sr diffusion coefficient compiled by Zellmer (2000), which is based on the experimental dataset (Giletti and Casserly, 1994):

$$D_{\mathrm{Sr}} = 2.92 \times 10^{(-4.1X_{\mathrm{An}}-4.08)} \exp\left(\frac{-276000}{RT}\right)$$

where D_{Sr} is the diffusion coefficient of Sr ($m^2\ s^{-1}$), X_{An} is the mole fraction of anorthite, R is the gas constant (8.314 J $mol^{-1}K^{-1}$), and T is absolute temperature (K). The initial Sr profile was inferred based on the analytical values interpreted as the undiffused zone. The equilibrium Sr profile was calculated using the outermost rim Sr concentration via the partition coefficients (Bindeman et al., 1998). The magmatic temperature was set to ~1025 °C. The diffusion modelling was performed using the equation considering the dependency on the An content of chemical potential (Costa et al., 2003):

$$\frac{\partial C_{\mathrm{Sr}}}{\partial t} = \frac{\partial}{\partial x}\left(D_{\mathrm{Sr}}\frac{\partial C_{\mathrm{Sr}}}{\partial x} - \frac{D_{\mathrm{Sr}}C_{\mathrm{Sr}}}{RT}A_{\mathrm{Sr}}\frac{\partial X_{\mathrm{An}}}{\partial x}\right)$$

where A_{Sr} is the slope of the partitioning relationship for Sr. X_{An} is the mole fraction of An content.

Sr diffusion modelling yielded timescales of 2 years for OKP_4-2-3 pl-19 and 11 years for OKP_5-2-1 pl-24. In comparison with CaAl–NaSi diffusion modelling applied to the same plagioclase crystal, Sr diffusion modelling results yielded longer timescales (Figure 6–Figure 8). Greyscale intensity profiles derived from BSE images indicate the presence of fine-scale zoning patterns (Supplementary Material). In contrast, owing to the limitation of spatial resolution, LA-ICP-MS analysis detects only large-scale compositional gradients in the Sr profiles. This difference in spatial resolution between BSE imaging (<0.1 μm) and LA-ICP-MS (>10 μm) may influence the discrepancy in diffusion modelling results.

4. Discussion

4.1. Rapid remobilization process

Previous geophysical and petrological studies have revealed a picture of the trans-crustal magma plumbing system beneath Zao Volcano (Figure 10a) (Okada et al., 2015; Ban et al., 2016; Zellmer et al., 2019; Sato et al., 2022; Ban et al., 2025; Sato et al., 2025). Basaltic magmas (M_1, ~50 mass% SiO_2), which are generated in hot zone within the lower crust (20–40 km in depth), recharged into the shallow reservoir (~8 km in depth) that consists of mushy andesitic magma (M_2, ~59 mass% SiO_2) and surrounding andesitic to dacitic magma (M_3, >60 mass% SiO_2).

The mineralogical features and diffusion timescales recorded by plagioclase crystals reconstruct a remobilization model for the shallow mush-dominated reservoir beneath Zao Volcano. The result of diffusion chronometry shows

a wide range of timescales that spans within one month to centuries before the eruption (Figure 9). The timescale results obtained crystal cores showed longer timescales than those of the rims (Figure 4Figure 9). The pre-eruptive short diffusion timescales obtained from the rim-ward boundaries (3–10 years) indicate a change in physicochemical conditions shortly before the eruption. An abrupt increase of An content and formation of the dusty-zoned mantle are associated with the magma mixing, accompanied by the mafic magma recharge before the eruption. Conversely, the long diffusion times obtained from the core-ward boundaries (>10 years). The maximum diffusion timescales likely reflect the starting times of mafic magma recharge.

The distribution of timescales increased progressively toward shorter timescales. The timescale <10 years constitutes >90% of the whole timescale results, and a half of plagioclase especially shows timescales within 1 years. The density of timescale distribution may be attributed to the frequency of recharge episodes. Higher densities at shorter timescales indicate increased rates of magma recharge and remobilization, whilst sporadic, longer timescales represent lower levels of recharge rates. Basaltic magma recharge into the shallow reservoir results in magma mixing and remobilization of the mush-dominated reservoir, thereby triggering eruption. The predominance of crystals with short timescales is consistent with timescale results obtained from Fe–Mg in orthopyroxene (Sato et al., 2022) and Mg in plagioclase (Sato et al., 2025). Such pre-eruptive mafic recharge episodes are mainly recorded by the formation of dusty-zoned mantle in plagioclase. The limited abundance of dusty-zoned plagioclase is interpreted to indicate that the direct mixing between recharging basaltic magma and pre-existing andesitic magma was spatially restricted. Plagioclase crystals exhibiting short timescales without dusty-zoned mantles are inferred to represent entrained crystals derived from disaggregated crystal mush, subsequently carried by sufficiently hybridized eruptive melt.

4.2. Multiple magma recharge episodes

Plagioclase crystals exhibiting complex zoning patterns record repeated magma recharge episodes, whilst those with simpler textures record sporadic recharge. From the perspective of crystal system analysis applied to plagioclase zoning patterns by Sato et al. (2025), textural complexity shows no systematic relationship with crystal origins inferred by plagioclase core textures. Instead, these textural characteristics are more consistent with an architecture of the shallow reservoir composed of spatially scattered melt batches rather than a single, compositionally and thermally stratified magma reservoir (Nakagawa et al., 2002; Sato et al., 2025). This strongly suggests that magma intrusion affects spatially restricted regions of the shallow reservoir. The existence of crystals showing hiatuses between mafic magma recharges also supports that the mafic magma intruded intermittently. Absence of temporal variation in the maximum timescales (Figure 9) suggests that spatially distinct regions were remobilized by mafic magma recharge during each subunit (Figure 10). Compared with a single, large magma chamber, small magma batches may be attributed to large thermal and chemical diversity driven by heat transfer and mixing ratio, resulting in the wide compositional range observed in plagioclase.

The Okp plagioclase zoning is governed predominantly by magma mixing induced by magma recharge (Sato et al., 2025). The large distribution of timescales represents multiple recharge episodes rather than a single event. The occurrence of multiple recharge episodes is supported qualitatively by the existence of complexly zoned plagioclase. Zoning complexity is defined as the total number of different zoning types present in a given crystal (Bennet et al.,

2019). The zoning of Okp plagioclase can be subdivided into as many as five zones based on dissolution boundaries. However, a single crystal does not necessarily record the entire sequence of recharge episodes. We constrained the minimum number of pre-eruptive recharge episodes by clustering the timescale distribution (Mangler et al., 2022). This approach successfully subdivided timescale distributions of pyroxene Fe–Mg interdiffusion timescales from Popocatépetl volcano into clusters based on their overlapping errors. Considering the uncertainty of diffusion modelling, the Okp timescale distribution can be subdivided into four to six recharge episodes (Figure 9c), which are comparable to those estimated from zoning complexity. The interval of mafic magma recharge estimated from the number of recharge episodes is approximately 10 years, which shows good agreement with the eruption interval determined from tephrochronological studies (Ban et al., 2015).

5. Conclusions

We investigated the long-term remobilization processes of the shallow magma reservoir during historical activity (*ca.* 1200 CE to the present) at Zao Volcano. Magma mixing accompanied with mafic magma recharge is recorded in the textures and compositional zoning of plagioclase crystals. The coexistence of simply and complexly zoned plagioclase indicates that these crystals record distinct pre-eruptive histories, suggesting that magma intrusion affected spatially restricted regions within the shallow reservoir (i.e. small magma batches). This model of small, remobilized magma batches is consistent with the sparse geophysical evidence for hot plutons beneath Zao Volcano. Diffusion chronometry, applied to CaAl–NaSi interdiffusion in plagioclase with high-resolution BSE imaging, enables the extraction of timescales associated with long-term recharge histories. The absence of systematic changes in the distribution of diffusion timescales supports the hypothesis that spatially distinct regions of the shallow reservoir were remobilized during each eruption. The distribution of diffusion timescales increases exponentially toward shorter durations, indicating intensified magma recharge immediately prior to eruption. This interpretation is consistent with diffusion timescales derived from other mineral phases (e.g. Mg in plagioclase, and Fe–Mg in orthopyroxene). The continuous and rapid increase in recharge frequency leading up to the eruption provides important constraints on pre-eruptive processes at active arc volcanoes and highlights the importance of continuous monitoring in assessing the likelihood and timing of future eruptions.

Author contributions

Motohiro Sato: Conceptualization, Data curation, Formal analysis, Investigation, Methodology, Software, Visualization, Writing – original draft, Writing – review & editing. **Masao Ban:** Funding acquisition, Investigation, Methodology, Project administration, Resources, Supervision, Writing – review & editing. **Ryuichi Shinjo:** Methodology, Resources, Writing – review & editing. **Ke-Han Song:** Data curation, Writing – review & editing. **Takashi Yuguchi:** Methodology, Resources, Writing – review & editing. **Tatsuya Adachi:** Data curation, Writing – review & editing. **Takumi Imura:** Methodology, Writing – review & editing.

Acknowledgements

The authors would like to thank Saori Ohmiya for providing the samples used in this research, Kazuo Nakashima for EPMA analysis, and Kae Tsunematsu for the knowledge of numerical simulation. The prefectural offices of

Miyagi and Yamagata provided permission to survey Zao National Park. This work was supported by the Ministry of Education, Culture, Sports, Science and Technology “Integrated Program for Next Generation Volcano Research and Human Resource Development” and by a Grant-in-Aid for Scientific Research from the Japan Society for the Promotion of Science to M. Ban (22K03732, 25K07413).

Data availability

The authors confirm that the data supporting the findings of this study are available within the article and its supplementary materials.

References

Annen, C., Blundy, J.D., Sparks, R.S.J., 2006. The genesis of intermediate and silicic magmas in deep crustal hot zones. Journal of Petrology 47, 505–539. https://doi.org/10.1093/petrology/egi084

Bachmann, O., Bergantz, G.W., 2006. Gas percolation in upper-crustal silicic crystal mushes as a mechanism for upward heat advection and rejuvenation of near-solidus magma bodies. Journal of Volcanology and Geothermal Research 149, 85–102. https://doi.org/10.1016/j.jvolgeores.2005.06.002

Ban, M., Kanno, S., Sato, M., Imura, T., Tsunematsu, K., Hasegawa, T., Ohba, T., 2026. Magma feeding system of the 1893 CE Meiji eruption of Azumayama Volcano, NE Japan. Earth Planets Space 78, 37. https://doi.org/10.1186/s40623-025-02356-w

Ban, M., Kimura, J.-I., Takahashi, T., Hirahara, Y., Ohba, T., Fujinawa, A., Hayashi, S., Yoshida, T., Miyazaki, T., Chan, Q., Senda, R., Vaglarov, B.S., Tatsumi, Y., 2025. The significant role of the mafic lower crust in the chemical diversity of arc magmas. Island Arc 34, e70033. https://doi.org/10.2139/ssrn.4889276

Ban, M., Oikawa, T., Yamasaki, S., 2015. Geological map of Zao volcano. Geological Map of Volcanoes 18, 1–8.

Ban, M., Takebe, Y., Adachi, T., Matsui, R., Nishi, Y., 2016. Eruption histories of Zao and Azuma volcanoes and their magma feeding systems for recent activities. Bulletin of the Earthquake Research Institute 91, 25–39. https://doi.org/10.15083/0000032405

Bindeman, I.N., Davis, A.M., Drake, M.J., 1998. Ion microprobe Study of plagioclase-basalt partition experiments at natural concentration levels of trace elements. Geochimica et Cosmochimica Acta 62, 1175–1193. https://doi.org/10.1016/S0016-7037(98)00047-7

Cashman, K.V., Blundy, J.D., 2013. Petrological cannibalism: the chemical and textural consequences of incremental magma body growth. Contrib Mineral Petrol 166, 703–729. https://doi.org/10.1007/s00410-013-0895-0

Cashman, K.V., Sparks, R.S.J., Blundy, J.D., 2017. Vertically extensive and unstable magmatic systems: A unified view of igneous processes. Science 355, eaag3055. https://doi.org/10.1126/science.aag3055

Costa, F., Chakraborty, S., Dohmen, R., 2003. Diffusion coupling between trace and major elements and a model for calculation of magma residence times using plagioclase. Geochimica et Cosmochimica Acta 67, 2189–2200. https://doi.org/10.1016/S0016-7037(02)01345-5

Costa, F., Morgan, D., 2010. Time constraints from chemical equilibration in magmatic crystals, in: Dosseto, A., Turner, S.P., Van Orman, J.A. (Eds.), Timescales of Magmatic Processes. Wiley, pp. 125–159. https://doi.org/10.1002/9781444328509.ch7

Crank, J., 1976. The mathematics of diffusion, 2. ed., reprint. ed. Clarendon Press, Oxford.

Deevsalar, R., Pan, Y., Shinjo, R., Milan, L., Song, K., Xiao, Q., Shakouri, M., Paterson, A.R.-L., Hu, Y., 2023. Redox evolution of differentiating hydrous basaltic magmas recorded by zircon and apatites in mafic cumulates: The case of the Malayer Plutonic Complex, Western Iran. Geochemistry 83, 125946. https://doi.org/10.1016/j.chemer.2022.125946

Dohmen, R., Chakraborty, S., 2007. Fe–Mg diffusion in olivine II: point defect chemistry, change of diffusion mechanisms and a model for calculation of diffusion coefficients in natural olivine. Phys Chem Minerals 34, 409–430. https://doi.org/10.1007/s00269-007-0158-6

Dohmen, R., Ter heege, J.H., Becker, H.-W., Chakraborty, S., 2016. Fe-Mg interdiffusion in orthopyroxene. American Mineralogist 101, 2210–2221. https://doi.org/10.2138/am-2016-5815

Faak, K., Chakraborty, S., Coogan, L.A., 2013. Mg in plagioclase: Experimental calibration of a new geothermometer and diffusion coefficients. Geochimica et Cosmochimica Acta 123, 195–217. https://doi.org/10.1016/j.gca.2013.05.009

Ganguly, J., Tazzoli, V., 1994. Fe2+-Mg interdiffusion in orthopyroxene: Retrieval from the data on intracrystalline exchange reaction. American Mineralogist 79, 930–937.

Giletti, B.J., Casserly, J.E.D., 1994. Strontium diffusion kinetics in plagioclase feldspars. Geochimica et Cosmochimica Acta 58, 3785–3793. https://doi.org/10.1016/0016-7037(94)90363-8

Grove, T.L., Baker, M.B., Kinzler, R.J., 1984. Coupled CaAl-NaSi diffusion in plagioclase feldspar: Experiments and applications to cooling rate speedometry. Geochimica et Cosmochimica Acta 48, 2113–2121. https://doi.org/10.1016/0016-7037(84)90391-0

Kawamoto, T., 1992. Dusty and honeycomb plagioclase: indicators of processes in the Uchino stratified magma chamber, Izu Peninsula, Japan. Journal of Volcanology and Geothermal Research 49, 191–208. https://doi.org/10.1016/0377-0273(92)90014-5

Kent, A.J.R., Darr, C., Koleszar, A.M., Salisbury, M.J., Cooper, K.M., 2010. Preferential eruption of andesitic magmas through recharge filtering. Nature Geosci 3, 631–636. https://doi.org/10.1038/ngeo924

Kimura, J.-I., Chang, Q., 2012. Origin of the suppressed matrix effect for improved analytical performance in determination of major and trace elements in anhydrous silicate samples using 200 nm femtosecond laser ablation sector-field inductively coupled plasma mass spectrometry. J. Anal. At. Spectrom. 27, 1549–1559. https://doi.org/10.1039/C2JA10344C

Liu, M., Yund, R.A., 1992. NaSi-CaAl interdiffusion in plagioclase. American Mineralogist 77, 275–283.

Mangler, M.F., Petrone, C.M., Prytulak, J., 2022. Magma recharge patterns control eruption styles and magnitudes at Popocatépetl volcano (Mexico). Geology 50, 366–370. https://doi.org/10.1130/G49365.1

Marsh, B.D., 1996. Solidification fronts and magmatic evolution. Mineral. mag. 60, 5–40. https://doi.org/10.1180/minmag.1996.060.398.03

Müller, T., Dohmen, R., Becker, H.W., ter Heege, J.H., Chakraborty, S., 2013. Fe–Mg interdiffusion rates in clinopyroxene: experimental data and implications for Fe–Mg exchange geothermometers. Contributions to Mineralogy and Petrology 166, 1563–1576. https://doi.org/10.1007/s00410-013-0941-y

Nakagawa, M., Wada, K., Wood, C.P., 2002. Mixed magmas, mush chambers and eruption triggers: evidence from zoned clinopyroxene phenocrysts in andesitic scoria from the 1995 eruptions of Ruapehu volcano, New Zealand. Journal of Petrology 43, 2279–2303. https://doi.org/10.1093/petrology/43.12.2279

Okada, T., Matsuzawa, T., Umino, N., Yoshida, K., Hasegawa, A., Takahashi, H., Yamada, T., Kosuga, M., Takeda, T., Kato, A., Igarashi, T., Obara, K., Sakai, S., Saiga, A., Iidaka, T., Iwasaki, T., Hirata, N., Tsumura, N., Yamanaka, Y., Terakawa, T., Nakamichi, H., Okuda, T., Horikawa, S., Katao, H., Miura, T., Kubo, A., Matsushima, T., Goto, K., Miyamachi, H., 2015. Hypocenter migration and crustal seismic velocity distribution observed for the inland earthquake swarms induced by the 2011 Tohoku-Oki earthquake in NE Japan: implications for crustal fluid distribution and crustal permeability. Geofluids 15, 293–309. https://doi.org/10.1111/gfl.12112

Putirka, K.D., 2008. Thermometers and barometers for volcanic systems. Reviews in Mineralogy and Geochemistry 69, 61–120. https://doi.org/10.2138/rmg.2008.69.3

Rubin, A.E., Cooper, K.M., Till, C.B., Kent, A.J.R., Costa, F., Bose, M., Gravley, D., Deering, C., Cole, J., 2017. Rapid cooling and cold storage in a silicic magma reservoir recorded in individual crystals. Science 356, 1154–1156. https://doi.org/10.1126/science.aam8720

Sato, M., Ban, M., Yuguchi, T., Adachi, T., 2022. Pre-eruptive magmatic processes of historical activities at Zao volcano, northeastern Japan: Insights from compositional zoning in orthopyroxene phenocrysts. Journal of Volcanology and Geothermal Research 432, 107686. https://doi.org/10.1016/j.jvolgeores.2022.107686

Sato, M., Ban, M., Yuguchi, T., Adachi, T., Imura, T., Takebe, M., 2025. Mush remobilisation process during historical activity at the Zao volcano, northeastern Japan: Perspectives from plagioclase textures and compositions. Journal of Volcanology and Geothermal Research 108458. https://doi.org/10.1016/j.jvolgeores.2025.108458

Sparks, R.S.J., Sigurdsson, H., Wilson, L., 1977. Magma mixing: a mechanism for triggering acid explosive eruptions. Nature 267, 315–318. https://doi.org/10.1038/267315a0

Tsuchiyama, A., 1985. Dissolution kinetics of plagioclase in the melt of the system diopside-albite-anorthite, and origin of dusty plagioclase in andesites. Contr. Mineral. and Petrol. 89, 1–16. https://doi.org/10.1007/BF01177585

Van Orman, J.A., Cherniak, D.J., Kita, N.T., 2014. Magnesium diffusion in plagioclase: Dependence on composition, and implications for thermal resetting of the 26Al–26Mg early solar system chronometer. Earth and Planetary Science Letters 385, 79–88. https://doi.org/10.1016/j.epsl.2013.10.026

Van Orman, J.A., Crispin, K.L., 2010. Diffusion in Oxides. Reviews in Mineralogy and Geochemistry 72, 757–825. https://doi.org/10.2138/rmg.2010.72.17

Viccaro, M., Giacomoni, P.P., Ferlito, C., Cristofolini, R., 2010. Dynamics of magma supply at Mt. Etna volcano (Southern Italy) as revealed by textural and compositional features of plagioclase phenocrysts. Lithos 116, 77–91. https://doi.org/10.1016/j.lithos.2009.12.012

Zellmer, G.F., 2021. Gaining acuity on crystal terminology in volcanic rocks. Bull Volcanol 83, 78. https://doi.org/10.1007/s00445-021-01505-9

Zellmer, G.F., Chen, K.-X., Gung, Y., Kuo, B.-Y., Yoshida, T., 2019. Magma transfer processes in the NE Japan arc: Insights from crustal ambient noise tomography combined with volcanic eruption records. Front. Earth Sci. 7, 40. https://doi.org/10.3389/feart.2019.00040

Zhang, C., Koepke, J., Kirchner, C., Götze, N., Behrens, H., 2015. Rapid hydrothermal cooling above the axial melt lens at fast-spreading mid-ocean ridge. Sci Rep 4, 6342. https://doi.org/10.1038/srep06342

Tables

Table 1: Timescale results from plagioclase CaAl–NaSi diffusion modelling.

Subunit	Location	Sample	Crystal No.	Line	t (day)	t (year)	Type	Relative distance
Okp-1	Loc. 1	OKP_4-1-1	pl-02	1_1	50	0.1	B	1
Okp-1	Loc. 1	OKP_4-1-1	pl-02	1_2	300	0.8	B	3
Okp-1	Loc. 1	OKP_4-1-1	pl-02	1_3	100	0.3	B	2
Okp-1	Loc. 1	OKP_4-1-1	pl-02	1_4	600	1.6	B	3
Okp-1	Loc. 1	OKP_4-1-1	pl-02	2_1	200	0.5	B	1
Okp-1	Loc. 1	OKP_4-1-1	pl-02	2_2	100	0.3	B	1
Okp-1	Loc. 1	OKP_4-1-1	pl-02	2_3	800	2.2	B	2
Okp-1	Loc. 1	OKP_4-1-1	pl-08	1_1	30	0.1	B	1
Okp-1	Loc. 1	OKP_4-1-1	pl-08	1_2	300	0.8	B	2
Okp-1	Loc. 1	OKP_4-1-1	pl-08	1_3	100	0.3	B	2
Okp-1	Loc. 1	OKP_4-1-1	pl-08	1_4	200	0.5	B	3
Okp-1	Loc. 1	OKP_4-1-1	pl-10	1_1	800	2.2	A	1
Okp-1	Loc. 1	OKP_4-1-1	pl-10	1_2	500	1.4	A	2
Okp-1	Loc. 1	OKP_4-1-1	pl-10	2_1	5000	13.7	A	3
Okp-1	Loc. 1	OKP_4-1-1	pl-10	2_2	500	1.4	A	4
Okp-1	Loc. 1	OKP_4-1-1	pl-11	1_1	10000	27.4	B	1
Okp-1	Loc. 1	OKP_4-1-1	pl-11	1_2	900	2.5	B	1
Okp-1	Loc. 1	OKP_4-1-1	pl-17	1_1	30	0.1	C	1
Okp-1	Loc. 1	OKP_4-1-1	pl-17	1_2	1200	3.3	C	2
Okp-2	Loc. 1	OKP_4-2-3	pl-02	1_1	1800	4.9	C	5
Okp-2	Loc. 1	OKP_4-2-3	pl-02	1_2	9000	24.7	C	7
Okp-2	Loc. 1	OKP_4-2-3	pl-02	2_1	400	1.1	C	1
Okp-2	Loc. 1	OKP_4-2-3	pl-02	2_2	30	0.1	C	2
Okp-2	Loc. 1	OKP_4-2-3	pl-02	2_3	1200	3.3	C	3
Okp-2	Loc. 1	OKP_4-2-3	pl-02	2_4	4000	11.0	C	4
Okp-2	Loc. 1	OKP_4-2-3	pl-02	2_5	3500	9.6	C	5
Okp-2	Loc. 1	OKP_4-2-3	pl-02	2_6	2800	7.7	C	6
Okp-2	Loc. 1	OKP_4-2-3	pl-02	3_1	90	0.2	C	1
Okp-2	Loc. 1	OKP_4-2-3	pl-04	1_1	50	0.1	B	1
Okp-2	Loc. 1	OKP_4-2-3	pl-04	1_2	11000	30.1	B	2
Okp-2	Loc. 1	OKP_4-2-3	pl-04	1_3	550	1.5	B	3
Okp-2	Loc. 1	OKP_4-2-3	pl-04	2_1	500	1.4	B	2
Okp-2	Loc. 1	OKP_4-2-3	pl-04	2_2	1200	3.3	B	3
Okp-2	Loc. 1	OKP_4-2-3	pl-07	1_1	200	0.5	B	1
Okp-2	Loc. 1	OKP_4-2-3	pl-07	1_2	600	1.6	B	3
Okp-2	Loc. 1	OKP_4-2-3	pl-07	1_3	250	0.7	B	2
Okp-2	Loc. 1	OKP_4-2-3	pl-07	2_1	3800	10.4	B	2
Okp-2	Loc. 1	OKP_4-2-3	pl-07	2_2	300	0.8	B	4
Okp-2	Loc. 1	OKP_4-2-3	pl-07	2_3	4000	11.0	B	5
Okp-2	Loc. 1	OKP_4-2-3	pl-07	3_1	800	2.2	B	2
Okp-2	Loc. 1	OKP_4-2-3	pl-07	3_2	300	0.8	B	2
Okp-2	Loc. 1	OKP_4-2-3	pl-07	3_3	10000	27.4	B	4
Okp-2	Loc. 1	OKP_4-2-3	pl-08	1_1	150	0.4	C	3

Okp-2	Loc. 1	OKP_4-2-3	pl-08	1_2	50	0.1	C	4
Okp-2	Loc. 1	OKP_4-2-3	pl-08	1_3	450	1.2	C	5
Okp-2	Loc. 1	OKP_4-2-3	pl-08	1_4	900	2.5	C	6
Okp-2	Loc. 1	OKP_4-2-3	pl-08	1_5	5500	15.1	C	7
Okp-2	Loc. 1	OKP_4-2-3	pl-08	1_6	2000	5.5	C	8
Okp-2	Loc. 1	OKP_4-2-3	pl-08	3_1	600	1.6	C	1
Okp-2	Loc. 1	OKP_4-2-3	pl-08	3_2	2000	5.5	C	2
Okp-2	Loc. 1	OKP_4-2-3	pl-09	3_1	20	0.1	B	1
Okp-2	Loc. 1	OKP_4-2-3	pl-09	3_2	8000	21.9	B	2
Okp-2	Loc. 1	OKP_4-2-3	pl-10	1_1	50	0.1	D	1
Okp-2	Loc. 1	OKP_4-2-3	pl-13	1_1	60	0.2	C	1
Okp-2	Loc. 1	OKP_4-2-3	pl-17	1_1	30	0.1	B	1
Okp-2	Loc. 1	OKP_4-2-3	pl-17	1_2	10	0.0	B	2
Okp-2	Loc. 1	OKP_4-2-3	pl-17	1_3	80	0.2	B	3
Okp-2	Loc. 1	OKP_4-2-3	pl-17	1_4	200	0.5	B	4
Okp-2	Loc. 1	OKP_4-2-3	pl-17	1_5	600	1.6	B	5
Okp-2	Loc. 1	OKP_4-2-3	pl-17	2_1	450	1.2	B	6
Okp-2	Loc. 1	OKP_4-2-3	pl-17	2_2	500	1.4	B	7
Okp-2	Loc. 1	OKP_4-2-3	pl-18	1_1	9	0.0	B	1
Okp-2	Loc. 1	OKP_4-2-3	pl-18	1_2	50	0.1	B	2
Okp-2	Loc. 1	OKP_4-2-3	pl-18	1_3	30	0.1	B	3
Okp-2	Loc. 1	OKP_4-2-3	pl-18	1_4	400	1.1	B	4
Okp-2	Loc. 1	OKP_4-2-3	pl-18	1_5	1200	3.3	B	5
Okp-2	Loc. 1	OKP_4-2-3	pl-19	1_1	300	0.8	B	1
Okp-2	Loc. 1	OKP_4-2-3	pl-19	1_2	30	0.1	B	2
Okp-2	Loc. 1	OKP_4-2-3	pl-22	1_1	40	0.1	B	1
Okp-2	Loc. 1	OKP_4-2-3	pl-22	1_2	150	0.4	B	2
Okp-2	Loc. 1	OKP_4-2-3	pl-22	1_3	300	0.8	B	4
Okp-2	Loc. 1	OKP_4-2-3	pl-22	2_1	10	0.0	B	1
Okp-2	Loc. 1	OKP_4-2-3	pl-22	2_2	100	0.3	B	2
Okp-2	Loc. 1	OKP_4-2-3	pl-22	2_3	2000	5.5	B	3
Okp-2	Loc. 1	OKP_4-2-3	pl-22	2_4	1500	4.1	B	4
Okp-2	Loc. 1	OKP_4-2-3	pl-22	3_1	30	0.1	B	1
Okp-2	Loc. 1	OKP_4-2-3	pl-22	3_2	300	0.8	B	2
Okp-2	Loc. 1	OKP_4-2-3	pl-22	3_3	3500	9.6	B	2
Okp-2	Loc. 1	OKP_4-2-3	pl-24	1_1	5	0.0	D	1
Okp-2	Loc. 1	OKP_4-2-3	pl-24	1_2	180	0.5	D	2
Okp-3	Loc. 1	OKP_4-3-1	pl-01	1_1	200	0.5	B	1
Okp-3	Loc. 1	OKP_4-3-1	pl-01	2_1	300	0.8	B	2
Okp-3	Loc. 1	OKP_4-3-1	pl-02	1_1	900	2.5	B	1
Okp-3	Loc. 1	OKP_4-3-1	pl-03	1_1	700	1.9	B	1
Okp-3	Loc. 1	OKP_4-3-1	pl-03	2_1	200	0.5	B	2
Okp-3	Loc. 1	OKP_4-3-1	pl-03	2_2	700	1.9	B	3
Okp-3	Loc. 1	OKP_4-3-1	pl-04	1_1	700	1.9	A	1
Okp-3	Loc. 1	OKP_4-3-1	pl-04	1_2	10	0.0	A	2
Okp-3	Loc. 1	OKP_4-3-1	pl-04	1_3	500	1.4	A	3
Okp-3	Loc. 1	OKP_4-3-1	pl-06	1_1	300	0.8	C	1
Okp-3	Loc. 1	OKP_4-3-1	pl-06	1_2	2000	5.5	C	2

Okp-3	Loc. 1	OKP_4-3-1	pl-06	1_3	1200	3.3	C	3
Okp-3	Loc. 1	OKP_4-3-1	pl-06	1_4	2000	5.5	C	4
Okp-3	Loc. 1	OKP_4-3-1	pl-06	1_5	4000	11.0	C	5
Okp-3	Loc. 1	OKP_4-3-1	pl-08	1_1	80	0.2	B	1
Okp-3	Loc. 1	OKP_4-3-1	pl-11	1_1	30	0.1	B	1
Okp-3	Loc. 1	OKP_4-3-1	pl-11	1_2	200	0.5	B	2
Okp-3	Loc. 1	OKP_4-3-1	pl-14	1_1	25	0.1	B	1
Okp-3	Loc. 1	OKP_4-3-1	pl-14	1_2	300	0.8	B	2
Okp-3	Loc. 1	OKP_4-3-1	pl-14	1_3	700	1.9	B	2
Okp-3	Loc. 1	OKP_4-3-1	pl-14	2_1	6000	16.4	B	3
Okp-3	Loc. 1	OKP_4-3-1	pl-16	1_1	40	0.1	A	1
Okp-3	Loc. 1	OKP_4-3-1	pl-16	1_2	1900	5.2	A	2
Okp-3	Loc. 1	OKP_4-3-1	pl-16	1_3	500	1.4	A	3
Okp-3	Loc. 1	OKP_4-3-1	pl-16	1_4	350	1.0	A	4
Okp-3	Loc. 1	OKP_4-3-1	pl-16	1_5	1100	3.0	A	5
Okp-3	Loc. 1	OKP_4-3-1	pl-16	2_1	350	1.0	A	6
Okp-3	Loc. 1	OKP_4-3-1	pl-16	2_2	350	1.0	A	7
Okp-3	Loc. 1	OKP_4-3-1	pl-16	2_3	700	1.9	A	8
Okp-3	Loc. 1	OKP_4-3-1	pl-16	2_4	6000	16.4	A	9
Okp-3	Loc. 1	OKP_4-3-1	pl-18	1_1	6000	16.4	C	1
Okp-3	Loc. 1	OKP_4-3-1	pl-18	1_2	50000	137.0	C	2
Okp-4	Loc. 1	OKP_4-4-3	pl-01	1_1	20	0.1	B	1
Okp-4	Loc. 1	OKP_4-4-3	pl-01	1_2	80	0.2	B	1
Okp-4	Loc. 1	OKP_4-4-3	pl-02	1_1	1000	2.7	B	1
Okp-4	Loc. 1	OKP_4-4-3	pl-02	1_3	1200	3.3	B	2
Okp-4	Loc. 1	OKP_4-4-3	pl-03	1_1	15	0.0	B	1
Okp-4	Loc. 1	OKP_4-4-3	pl-03	1_2	210	0.6	B	2
Okp-4	Loc. 1	OKP_4-4-3	pl-03	1_3	200	0.5	B	3
Okp-4	Loc. 1	OKP_4-4-3	pl-03	1_4	130	0.4	B	4
Okp-4	Loc. 1	OKP_4-4-3	pl-03	1_5	90	0.2	B	5
Okp-4	Loc. 1	OKP_4-4-3	pl-03	1_6	60	0.2	B	6
Okp-4	Loc. 1	OKP_4-4-3	pl-04	1_1	20	0.1	B	1
Okp-4	Loc. 1	OKP_4-4-3	pl-04	1_2	3000	8.2	B	2
Okp-4	Loc. 1	OKP_4-4-3	pl-04	1_3	30000	82.2	B	3
Okp-4	Loc. 1	OKP_4-4-3	pl-06	1_1	90	0.2	D	1
Okp-4	Loc. 1	OKP_4-4-3	pl-06	2_1	1000	2.7	D	2
Okp-4	Loc. 1	OKP_4-4-3	pl-06	2_2	600	1.6	D	3
Okp-4	Loc. 1	OKP_4-4-3	pl-07	1_1	9000	24.7	B	2
Okp-4	Loc. 1	OKP_4-4-3	pl-07	1_2	3000	8.2	B	3
Okp-4	Loc. 1	OKP_4-4-3	pl-07	3_1	600	1.6	B	1
Okp-4	Loc. 1	OKP_4-4-3	pl-08	2_1	900	2.5	A	2
Okp-4	Loc. 1	OKP_4-4-3	pl-08	3_1	25	0.1	A	1
Okp-4	Loc. 1	OKP_4-4-3	pl-08	3_2	800	2.2	A	3
Okp-4	Loc. 1	OKP_4-4-3	pl-08	3_3	70	0.2	A	4
Okp-4	Loc. 1	OKP_4-4-3	pl-09	1_1	1000	2.7	A	3
Okp-4	Loc. 1	OKP_4-4-3	pl-09	1_2	300	0.8	A	4
Okp-4	Loc. 1	OKP_4-4-3	pl-09	1_3	300	0.8	A	7
Okp-4	Loc. 1	OKP_4-4-3	pl-09	1_4	500	1.4	A	8

Okp-4	Loc. 1	OKP_4-4-3	pl-09	2_1	600	1.6	A	2
Okp-4	Loc. 1	OKP_4-4-3	pl-09	2_2	600	1.6	A	3
Okp-4	Loc. 1	OKP_4-4-3	pl-09	2_3	5000	13.7	A	5
Okp-4	Loc. 1	OKP_4-4-3	pl-09	2_4	1000	2.7	A	6
Okp-4	Loc. 1	OKP_4-4-3	pl-09	3_1	70	0.2	A	1
Okp-4	Loc. 1	OKP_4-4-3	pl-10	1_1	1800	4.9	D	2
Okp-4	Loc. 1	OKP_4-4-3	pl-10	1_2	60	0.2	D	1
Okp-4	Loc. 1	OKP_4-4-3	pl-13	1_1	170	0.5	B	1
Okp-4	Loc. 1	OKP_4-4-3	pl-13	1_2	100	0.3	B	2
Okp-4	Loc. 1	OKP_4-4-3	pl-13	1_3	70	0.2	B	3
Okp-4	Loc. 1	OKP_4-4-3	pl-13	1_4	2000	5.5	B	4
Okp-4	Loc. 1	OKP_4-4-3	pl-13	1_5	1600	4.4	B	5
Okp-4	Loc. 1	OKP_4-4-3	pl-13	1_6	1200	3.3	B	6
Okp-4	Loc. 1	OKP_4-4-3	pl-21	1_1	800	2.2	B	2
Okp-4	Loc. 1	OKP_4-4-3	pl-21	1_2	700	1.9	B	3
Okp-4	Loc. 1	OKP_4-4-3	pl-21	2_1	170	0.5	B	1
Okp-4	Loc. 1	OKP_4-4-3	pl-21	2_2	1800	4.9	B	3
Okp-5	Loc. 2	OKP_16082606-1	pl-03	1_1	40	0.1	C	1
Okp-5	Loc. 2	OKP_16082606-1	pl-03	1_2	160	0.4	C	2
Okp-5	Loc. 2	OKP_16082606-1	pl-03	1_3	60	0.2	C	3
Okp-5	Loc. 2	OKP_16082606-1	pl-03	1_4	400	1.1	C	4
Okp-5	Loc. 2	OKP_16082606-1	pl-03	1_5	600	1.6	C	5
Okp-5	Loc. 2	OKP_16082606-1	pl-03	1_6	400	1.1	C	6
Okp-5	Loc. 2	OKP_16082606-1	pl-05	1_1	7000	19.2	C	5
Okp-5	Loc. 2	OKP_16082606-1	pl-05	2_1	600	1.6	C	1
Okp-5	Loc. 2	OKP_16082606-1	pl-05	2_2	450	1.2	C	2
Okp-5	Loc. 2	OKP_16082606-1	pl-05	2_3	600	1.6	C	3
Okp-5	Loc. 2	OKP_16082606-1	pl-05	2_4	500	1.4	C	4
Okp-5	Loc. 2	OKP_16082606-1	pl-05	2_5	4000	11.0	C	5
Okp-5	Loc. 2	OKP_16082606-1	pl-07	1_1	500	1.4	B	1
Okp-5	Loc. 2	OKP_16082606-1	pl-12	1_1	40	0.1	D	1
Okp-5	Loc. 2	OKP_16082606-1	pl-12	2_1	50	0.1	D	1
Okp-5	Loc. 2	OKP_16082606-1	pl-12	3_1	280	0.8	D	1
Okp-5	Loc. 2	OKP_16082606-1	pl-18	1_1	200	0.5	B	1
Okp-5	Loc. 2	OKP_16082606-1	pl-18	1_2	7000	19.2	B	2
Okp-5	Loc. 2	OKP_16082606-1	pl-18	1_3	700	1.9	B	3
Okp-5	Loc. 2	OKP_16082606-1	pl-18	1_4	1700	4.7	B	4
Okp-5	Loc. 2	OKP_16082606-1	pl-18	2_1	1900	5.2	B	5
Okp-5	Loc. 2	OKP_16082606-1	pl-18	2_2	9000	24.7	B	6
Okp-5	Loc. 2	OKP_16082606-1	pl-19	1_1	80	0.2	A	1
Okp-5	Loc. 2	OKP_16082606-1	pl-19	1_2	1000	2.7	A	2
Okp-5	Loc. 2	OKP_16082606-1	pl-19	1_3	4000	11.0	A	3
Okp-5	Loc. 2	OKP_16082606-1	pl-19	1_4	600	1.6	A	4
Okp-5	Loc. 2	OKP_16082606-1	pl-19	1_5	500	1.4	A	5
Okp-5	Loc. 2	OKP_16082606-1	pl-19	1_6	400	1.1	A	6
Okp-5	Loc. 2	OKP_16082606-1	pl-19	1_7	1800	4.9	A	7
Okp-5	Loc. 2	OKP_16082606-1	pl-19	1_8	2500	6.8	A	8
Okp-5	Loc. 2	OKP_16082606-1	pl-19	1_9	2000	5.5	A	9

Okp-5	Loc. 2	OKP_16082606-1	pl-19	2_1	80	0.2	A	2
Okp-5	Loc. 2	OKP_16082606-1	pl-19	2_2	350	1.0	A	3
Okp-5	Loc. 2	OKP_16082606-1	pl-19	2_3	480	1.3	A	4
Okp-5	Loc. 2	OKP_16082606-1	pl-19	2_4	650	1.8	A	5
Okp-5	Loc. 2	OKP_16082606-1	pl-19	2_5	45	0.1	A	6
Okp-5	Loc. 2	OKP_16082606-1	pl-19	2_6	2500	6.8	A	7
Okp-5	Loc. 2	OKP_16082606-1	pl-19	2_7	900	2.5	A	9
Okp-5	Loc. 2	OKP_16082606-1	pl-21	1_1	600	1.6	C	1
Okp-5	Loc. 2	OKP_16082606-1	pl-21	1_2	3000	8.2	C	4
Okp-5	Loc. 2	OKP_16082606-1	pl-21	2_1	6	0.0	C	2
Okp-5	Loc. 2	OKP_16082606-1	pl-21	2_2	700	1.9	C	3
Okp-5	Loc. 2	OKP_16082606-1	pl-22	1_1	25	0.1	B	1
Okp-5	Loc. 2	OKP_16082606-1	pl-22	1_2	250	0.7	B	2
Okp-5	Loc. 2	OKP_16082606-1	pl-22	1_3	180	0.5	B	3
Okp-5	Loc. 2	OKP_16082606-1	pl-22	1_4	120	0.3	B	4
Okp-5	Loc. 2	OKP_16082606-1	pl-22	2_1	300	0.8	B	5
Okp-5	Loc. 2	OKP_16082606-1	pl-22	2_2	300	0.8	B	6
Okp-6	Loc. 3a	OKP_5-2-1	pl-02	1_1	6000	16.4	B	1
Okp-6	Loc. 3a	OKP_5-2-1	pl-03	1_1	30	0.1	B	1
Okp-6	Loc. 3a	OKP_5-2-1	pl-03	1_2	150	0.4	B	2
Okp-6	Loc. 3a	OKP_5-2-1	pl-03	1_3	300	0.8	B	3
Okp-6	Loc. 3a	OKP_5-2-1	pl-03	1_4	800	2.2	B	5
Okp-6	Loc. 3a	OKP_5-2-1	pl-03	3_1	20	0.1	B	1
Okp-6	Loc. 3a	OKP_5-2-1	pl-03	3_2	2500	6.8	B	5
Okp-6	Loc. 3a	OKP_5-2-1	pl-03	3_3	25	0.1	B	4
Okp-6	Loc. 3a	OKP_5-2-1	pl-04	1_1	200	0.5	B	2
Okp-6	Loc. 3a	OKP_5-2-1	pl-04	1_2	150	0.4	B	3
Okp-6	Loc. 3a	OKP_5-2-1	pl-04	2_1	400	1.1	B	1
Okp-6	Loc. 3a	OKP_5-2-1	pl-04	2_2	1100	3.0	B	2
Okp-6	Loc. 3a	OKP_5-2-1	pl-08	1_1	2000	5.5	C	1
Okp-6	Loc. 3a	OKP_5-2-1	pl-08	1_2	1300	3.6	C	2
Okp-6	Loc. 3a	OKP_5-2-1	pl-08	1_3	400	1.1	C	3
Okp-6	Loc. 3a	OKP_5-2-1	pl-09	1_1	50	0.1	B	1
Okp-6	Loc. 3a	OKP_5-2-1	pl-09	1_2	150	0.4	B	2
Okp-6	Loc. 3a	OKP_5-2-1	pl-09	1_3	300	0.8	B	3
Okp-6	Loc. 3a	OKP_5-2-1	pl-09	1_4	400	1.1	B	4
Okp-6	Loc. 3a	OKP_5-2-1	pl-24	1_1	600	1.6	D	4
Okp-6	Loc. 3a	OKP_5-2-1	pl-24	1_2	900	2.5	D	5
Okp-6	Loc. 3a	OKP_5-2-1	pl-24	2_1	50	0.1	D	1
Okp-6	Loc. 3a	OKP_5-2-1	pl-24	2_2	170	0.5	D	2
Okp-6	Loc. 3a	OKP_5-2-1	pl-24	2_3	100	0.3	D	3

Figures

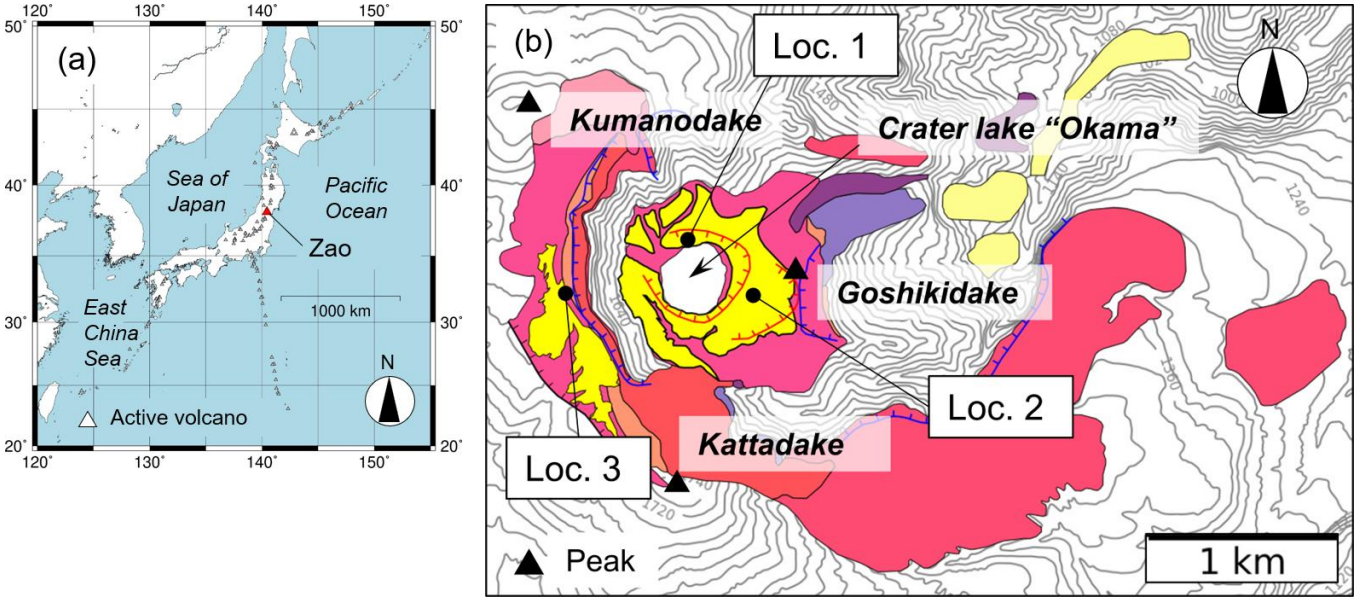

380 **Figure 1: Simplified geological map of the central part of Zao volcano (Modified from Sato et al., 2022). Black filled triangles show peaks. Yellow shaded areas show the distribution of Okama pyroclastics (Okp). Loc. 1 to 3 indicates the sampling points.**

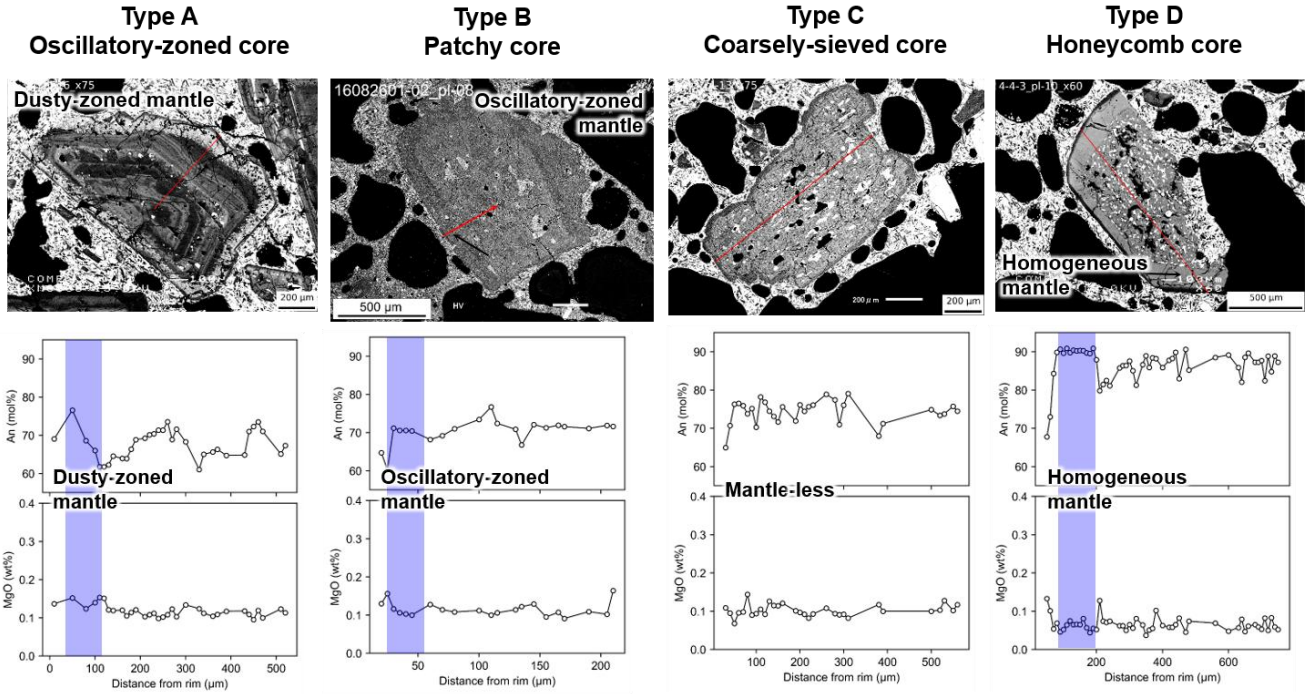

385 **Figure 2: BSE images and zoning profiles of An and MgO for the selected plagioclase phenocrysts. (a) Type A, oscillatory-zoned core plagioclase surrounded by the dusty-zoned mantle. (b) Type B, patchy core plagioclase surrounded by the oscillatory-zoned mantle. (c) Type C, coarsely-sieved core plagioclase. (d) Type D, honeycomb core plagioclase surrounded by the homogeneous An-rich mantles. All plagioclase phenocrysts are overgrown by the homogeneous An-poor rims.**

390

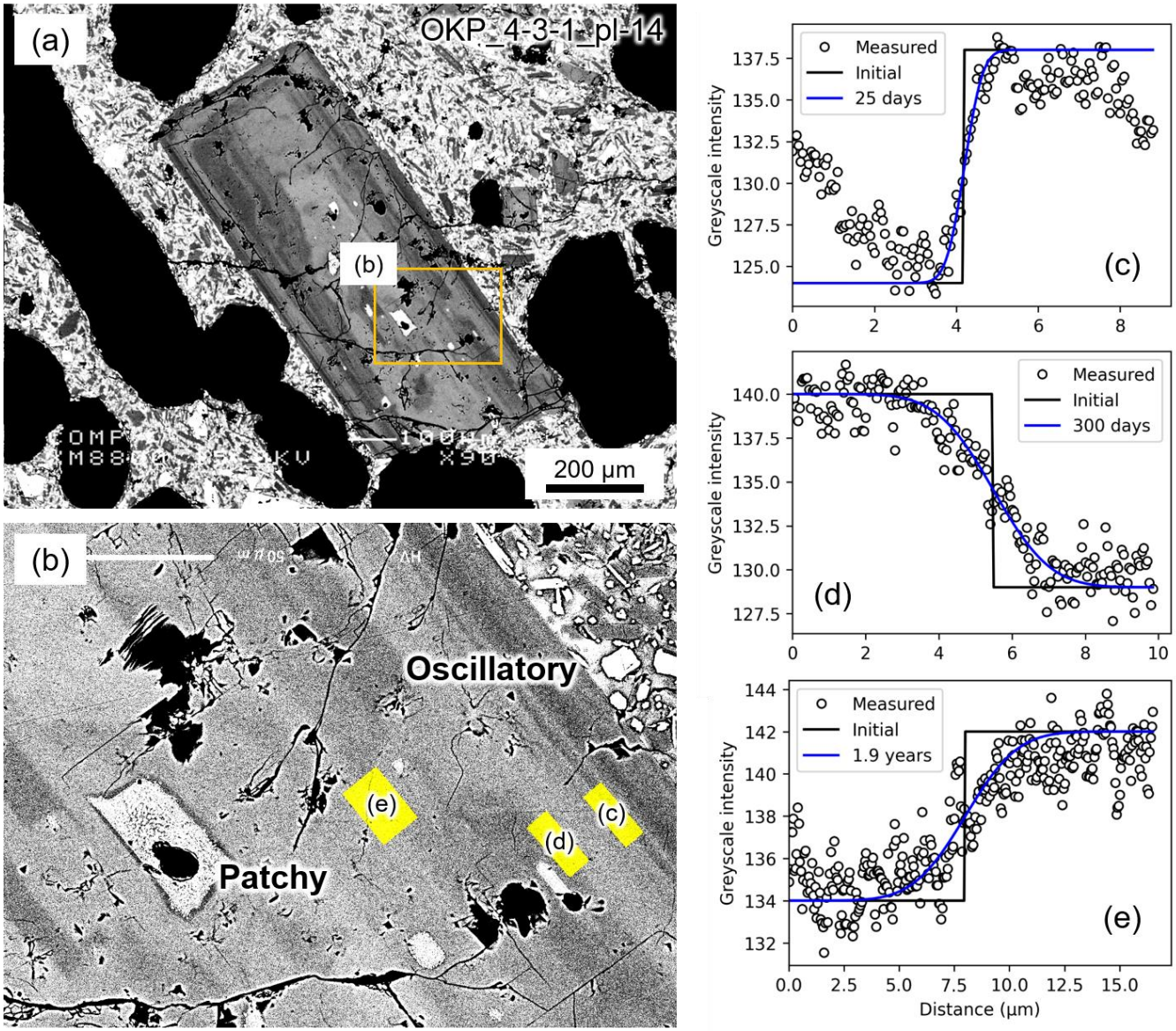

Figure 3: Modelling examples of CaAl-NaSi interdiffusion in plagioclase crystals (Type B, patchy core + oscillatory-zoned mantle + homogeneous rim). (a) Back-scattered electron (BSE) image, (b) magnified image, and (c–e) greyscale intensity (white circles), initial (black lines) and best-fit diffusion (blue lines) profiles.

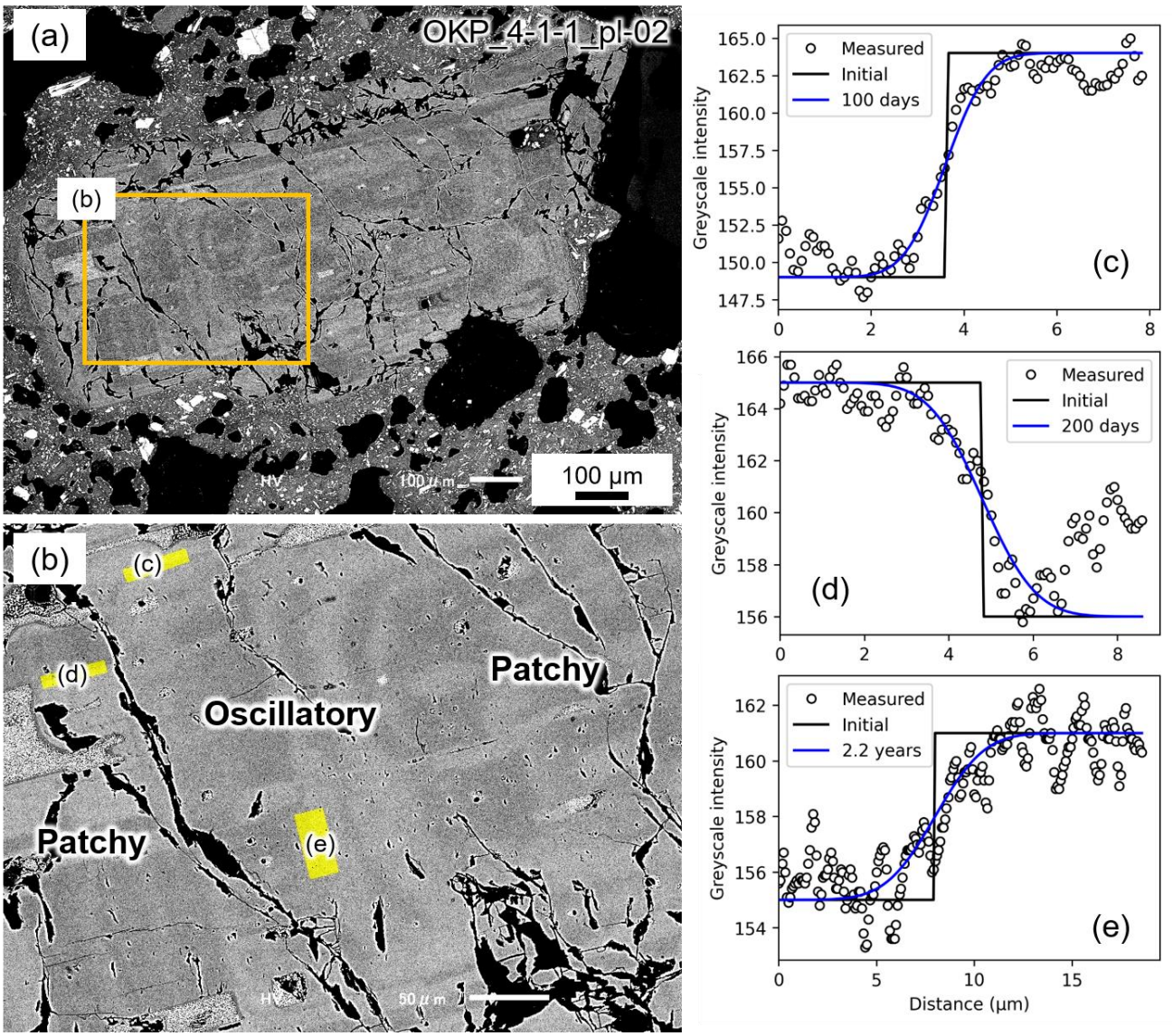

Figure 4: Modelling examples of CaAl-NaSi interdiffusion in plagioclase crystals (Type B, patchy core + oscillatory-zoned mantle + homogeneous rim). (a) Back-scattered electron (BSE) image, (b) magnified image, and (c–e) greyscale intensity (white circles), initial (black lines) and best-fit diffusion (blue lines) profiles.

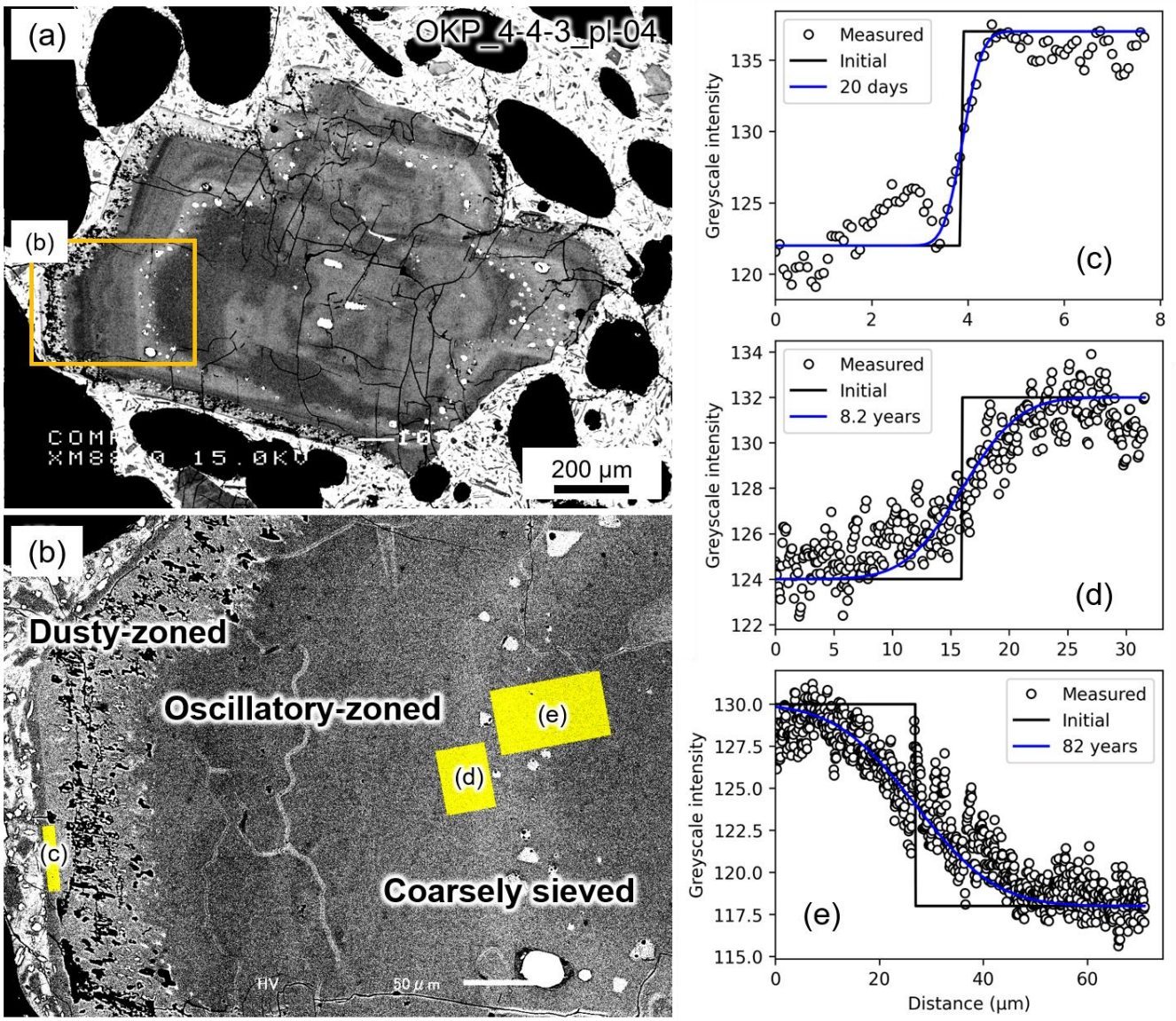

Figure 5: Modelling examples of CaAl-NaSi interdiffusion in plagioclase crystals (Type B, patchy core + coarsely sieved mantle + oscillatory-zoned mantle + dusty-zoned mantle + homogeneous rim). (a) Back-scattered electron (BSE) image, (b) magnified image, and (c–e) greyscale intensity (white circles), initial (black lines) and best-fit diffusion (blue lines) profiles.

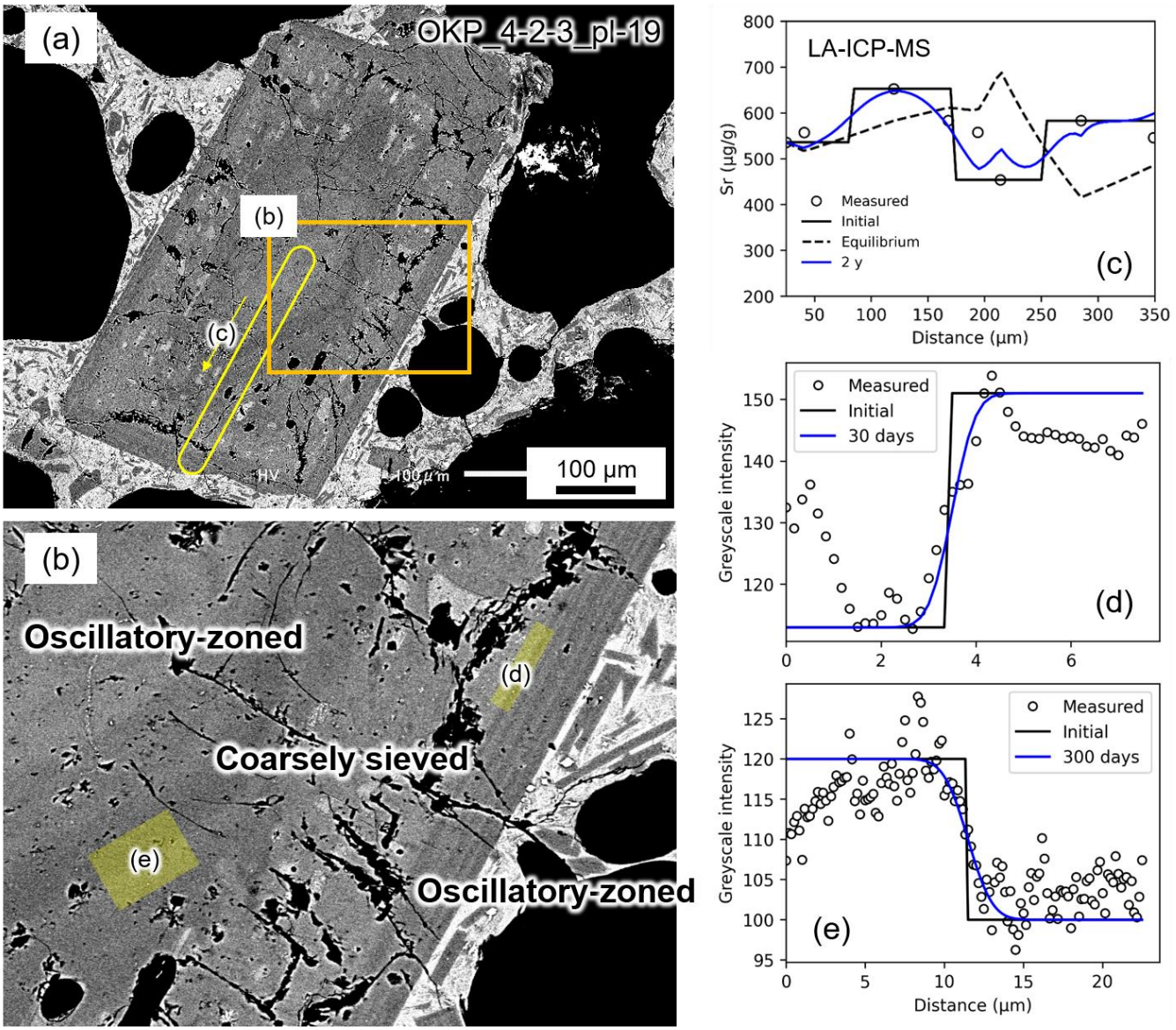

410 **Figure 6: Modelling examples of Sr diffusion and CaAl-NaSi interdiffusion in plagioclase crystals (Type A, oscillatory-zoned core + coarsely sieved mantle + oscillatory-zoned rim). (a) Back-scattered electron (BSE) image, (b) magnified image, (c) Sr profile, and (d–e) greyscale intensity (white circles), initial (black lines) and best-fit diffusion (blue lines) profiles.**

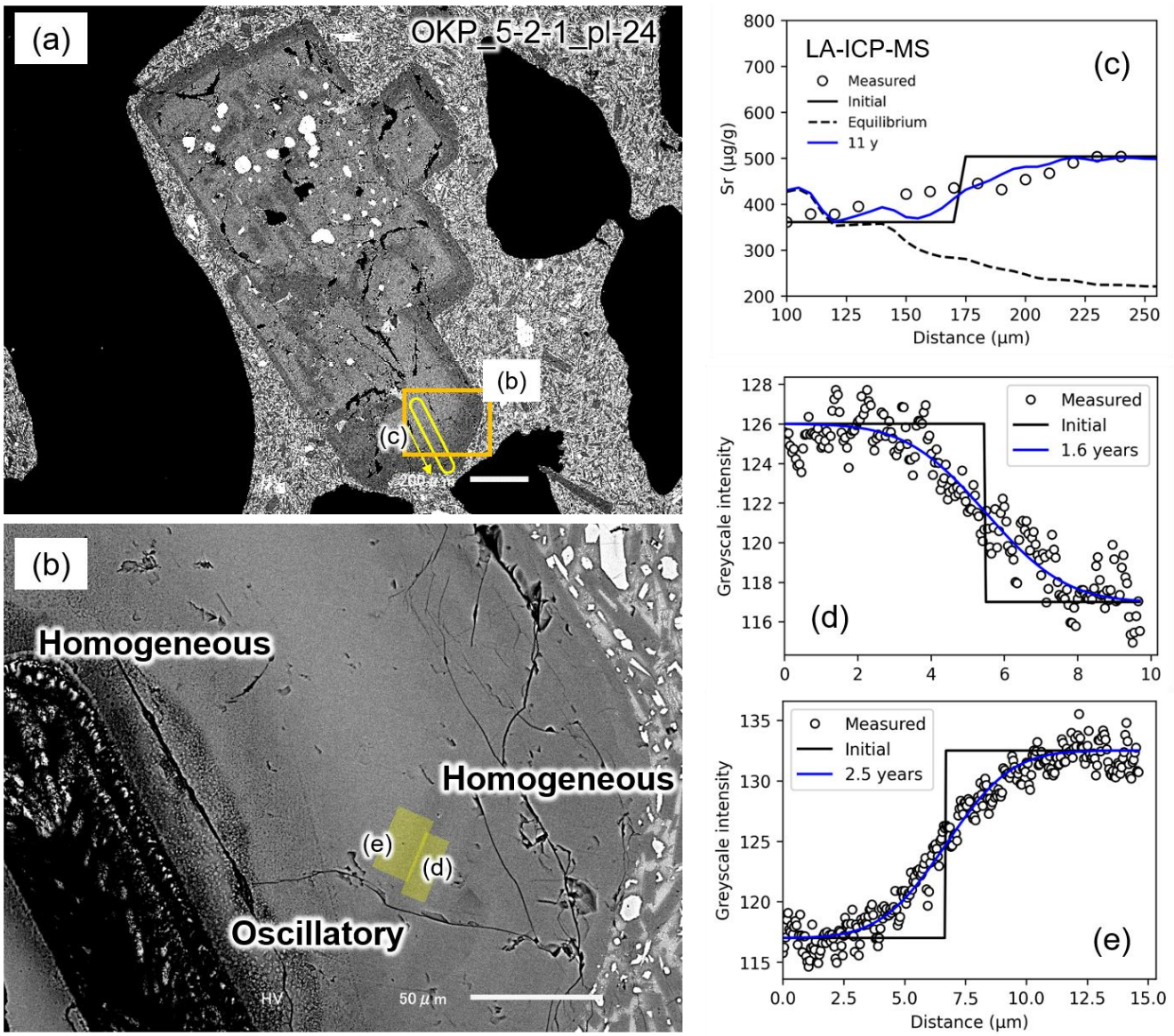

Figure 7: Modelling examples of Sr diffusion and CaAl-NaSi interdiffusion in plagioclase crystals (Type D, honeycomb core + homogeneous mantle + homogeneous rim). (a) Back-scattered electron (BSE) image, (b) magnified image, (c) Sr profile, and (d–e) greyscale intensity (white circles), initial (black lines) and best-fit diffusion (blue lines) profiles.

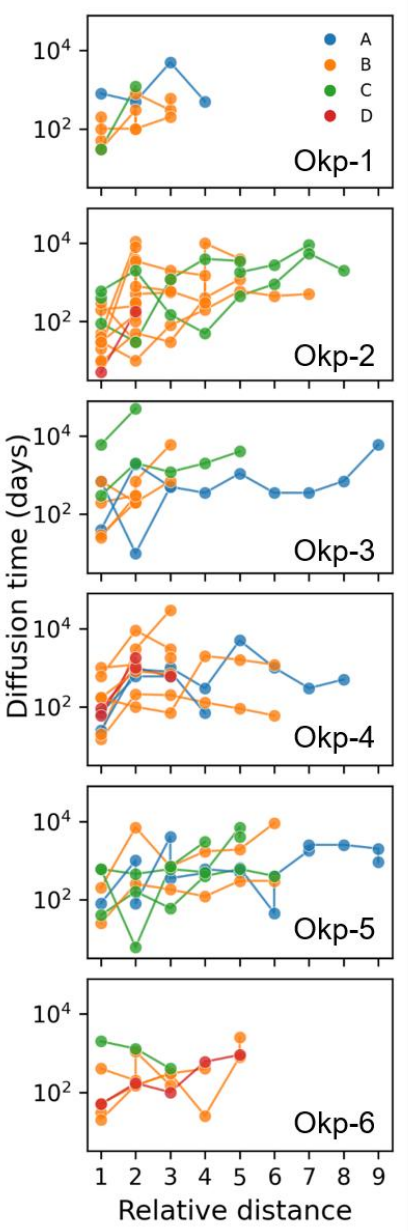

Figure 8: Relationship between diffusion times and the relative distance of modelled boundaries. The relative distance represents the indices of modelled boundaries within each crystal, starting from one at the outermost boundary and increasing toward to the interior. Lines connect diffusion times obtained from the same crystal. For clarity, only crystals containing two or more diffusion times within a single crystal are plotted. Diffusion times generally increases from the outer boundary toward the interior within a single crystal.

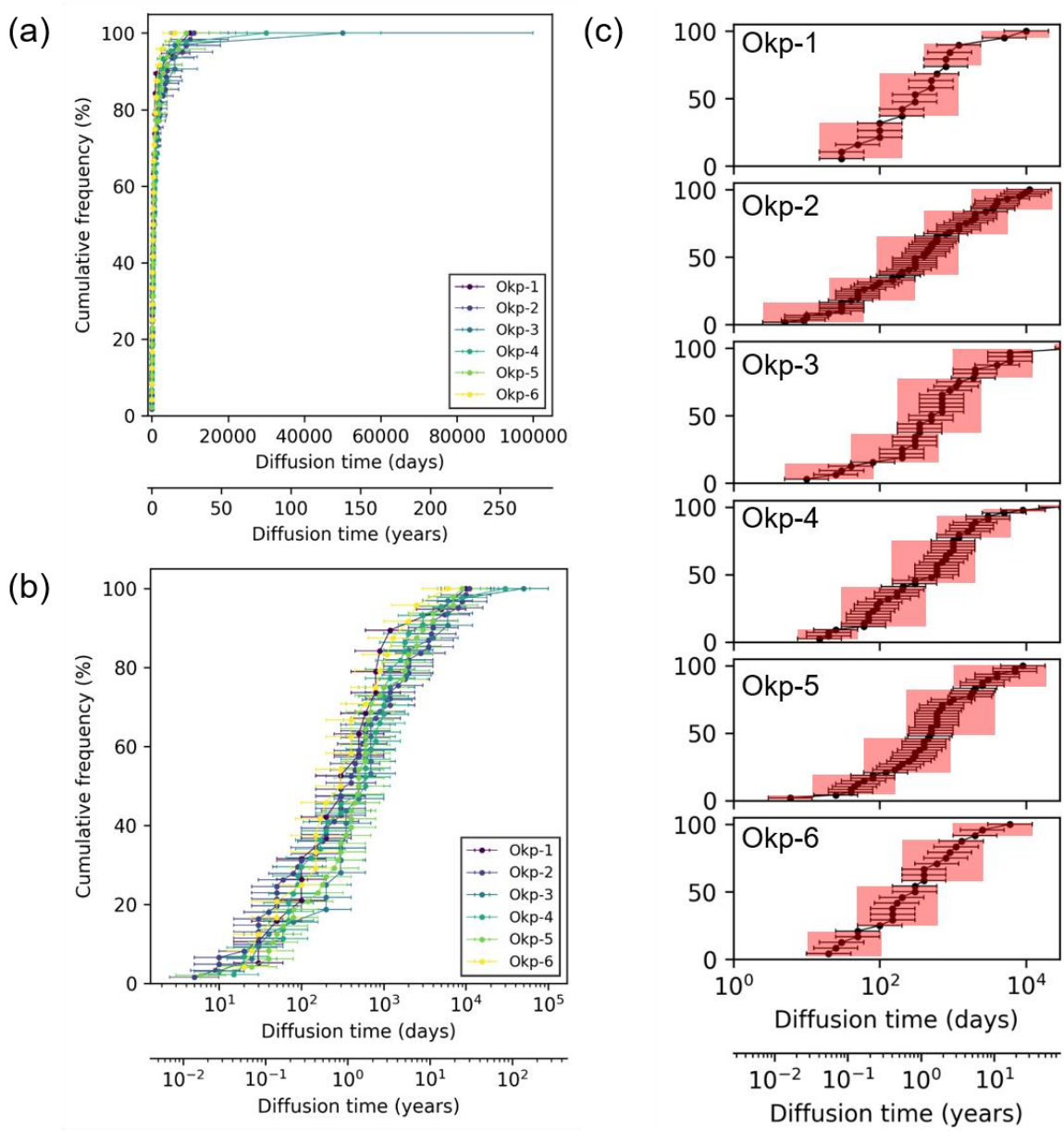

Figure 9: Distribution of diffusion modelling results. (a) Linear time, (b) Log time. (c) The temporal variation in the diffusion time results. For all subunits, short timescales were increased with time. The longest diffusion time was not systematically varied with time elapse, suggesting the past-crystallized plagioclase phenocrysts were not erupted. The lower limitation of modelling results estimated from the diffused width is less than 0.5 µm. As shown in the "Materials and methods" section, the spatial resolution of BSE images was ~0.1 µm at magnification of 500x. Red shaded boxes show individual recharge episodes defined by overlapping uncertainties based on the approach of Mangler et al. (2022).

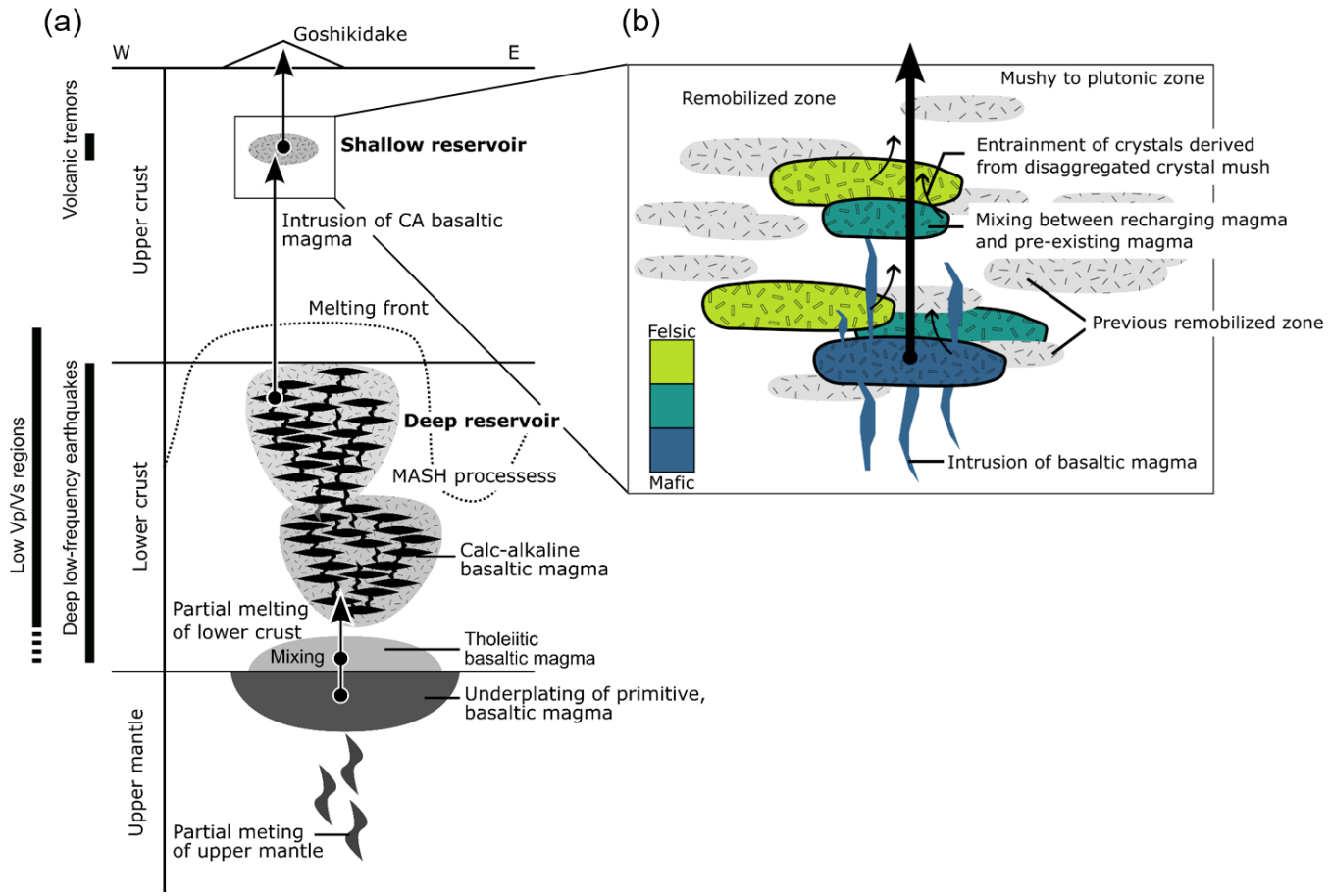

Figure 10: Schematic illustration of remobilization model of shallow reservoir beneath Zao Volcano. The main part of the reservoir is crystal-rich (crystal mush). The mushy reservoir partially remobilized by the recharged mafic magmas. The small-scale recharge events partially remobilize the mushy reservoir, generating many melt batches.